Electrical Engineering 84 (2002) 143–158 © Springer-Verlag 2002
DOI 10.1007/s00202-001-0113-3

A general nonlinear model of switched reluctance motor with mutual coupling and multiphase excitation

A. Deihimi, S. Farhangi, G. Henneberger

Abstract This paper presents a general nonlinear magnetic equivalent circuit model of a switched reluctance machine (SRM) that includes all possible flux paths in 2-D view of the machine, taking into account mutual coupling between phases and multiphase excitation. The model can be used to predict the performance of the machine with short or full pitched winding in static and dynamic regimes. Therefore, it is a simple analysing tool for finding the best configuration of SRM in computer-aided design and optimal design. A novel technique is employed to model the lumped elements of stator and rotor poles, and a new representation of the rotor core is introduced. Also, a general numerical matrix procedure is developed to calculate the total machine torque, and an approximate analytic alternative is presented. Inclusion of the rotor skew in the new model is described, and the accuracy of the model is verified by comparison of the simulation results with those obtained by the finite element method and measurements.

Keywords Switched reluctance machine, Magnetic equivalent circuit model, Multiphase excitation, Mutual coupling, Skewed rotor

List of symbols

A_p	cross-section area of a stator or rotor pole
a	cross-section area of a flux tube
a_j	cross-section area of a saturable flux tube defined in Eq. (1)
B	magnetic flux density
d_{sl}	parameter defined in Fig. 7a
g	airgap length
h_s	stator pole height
h_r	rotor pole height
H	magnetic field strength
I	phase current
i_i	current of the ith phase
J	current density
K_s, K_u	parameters defined in Eqs. (10) and (15), respectively
l_{stk}	rotor stack length
l_γ, l_λ	parameters defined in Fig. 11
l_v, r_v	parameters defined in Eqs. (19) and (20)
N_s	number of stator poles
N_r	number of rotor poles
N	number of winding turns per stator pole for each phase
N_{ph}	number of phases
P	magnetic permeance
R	phase resistance
$\mathbf{R}$	sub-matrix of the reluctance matrix
r_{sh}	shaft radius
r_{rb}	radius to the outer surface of the rotor yoke
r_{rp}	radius to the rotor pole tip
r_{sp}	radius to the stator pole tip
r_{sb}	radius to the inner surface of the stator yoke
r	radius parameter
T	total machine torque
V	DC input voltage of each phase
W_c	co-energy
W_f	magnetic stored energy
α	angle under each rotor pole defined in Fig. 4
β_s	stator pole arc
β_r	rotor pole arc
φ	magnetic flux within a flux tube or as a mesh flux related to the mesh analysis of the magnetic equivalent circuit
λ_θ, ω_θ, τ_θ	parameters defined in Fig. 12
λ_{max}	parameter defined in Eq. (32)
τ_r	parameter defined in Eq. (37)
ν	parameter defined in Fig. 7c
μ	magnetic permeability of saturable (iron) parts
μ_0	magnetic permeability of free space
θ	relative angle between a rotor pole and a nearby stator pole
θ_α	angle defined in Figs. 10 and 11
θ_{slot}	stator slot angle shown in Fig. 7
θ_{space}	angle shown in Fig. 11

Received: 6 December 2001/Accepted: 13 December 2001

A. Deihimi (✉), G. Henneberger
Department of Electrical Machines, RWTH Aachen,
Schinkel Str. 4, 52056 Aachen, Germany
e-mail: a_deihimi@yahoo.com
Tel.: +49-241-8097636; Fax: +49-241-8092270

S. Farhangi
Department of Electrical Engineering,
University of Tehran, North Kargar Ave,
PO Box 14395/515 Tehran, Iran

Second affiliation: A. Deihimi
Department of Electrical Engineering,
University of Tehran, North Kargar Ave,
PO Box 14395/515 Tehran, Iran

The authors would like to thank Dr. S. Risse for supplying the design and experimental data for the test machine, and also acknowledge the financial support made by the German Academic Exchange Service (DAAD) for this research.

ω_m	rotor angular speed
ξ_1, ξ_2	boundary angles between the three regions defined in Fig. 8
Ψ	magnetic flux linkage of a phase winding
ψ	magnetic flux within a stator pole
${}^k\psi$	magnetic flux within the kth slice of a stator pole
$\mathbf{F}$	mmf source matrix of the circuit mesh analysis in Eq. (52)
$\mathbf{I}_e$	unit diagonal matrix (all of diagonal elements equal to unity)
$\mathbf{Z}$	impedance or reluctance matrix of the circuit mesh analysis in Eq. (52)
$\mathbf{R}_{ij}$	sub-matrix of the reluctance matrix
Φ, Φ', Φ''	mesh flux vectors
Δf	width of the strips for the discrete integration in Eq. (66)
$\Delta\theta$	rotor angle increment

1 Introduction

While the switched reluctance machine (SRM) is very simple and cost effective in principle, it is rather difficult to design and develop performance predictions. Because of the highly saturated doubly salient pole structure of the SRM, most reliable results can be attained using advanced numerical methods such as the finite element method (FEM) [1–3]. Even with FEM, special techniques are required in order to obtain relatively accurate results [4]. However, the modeling and computational time of these methods is prohibitively large for dynamic analysis as well as for optimal design of SRM, where a large number of candidate designs must be evaluated in short design time frames.

As an alternative, some models of SRM have been developed based on known curves, which use empirical knowledge and need only a few precalculated points on the magnetization curves [5–7]. While these fast models are capable of taking into account all main nonlinearities due to saturation, they are unable to include the effects of mutual interactions between two or more simultaneously excited phases.

The magnetic equivalent circuit method, as another approach, has been used previously to model the saturated magnetic field of SRM [8–10]. Some important points based upon previous work and experience gained from the FEM results must be considered in order to develop an accurate and appropriate magnetic equivalent circuit model for the SRM.

First, normally saturated operation of the SRM causes high levels of saturation at corners of partially overlapping stator and rotor poles and results in sharp curving of the flux paths at the pole tips, as shown in Fig. 1. Thus, a specially refined model should be used for stator and rotor pole tips, and the nearby airgap [8].

Secondly, the required smooth torque for high-performance SRM drives makes the machine operate with overlap between exciting zones of successive phases, and consequently leads to the simultaneous excitation of two or more phases. The multiphase excitation of SRM may cause saturation of the stator and rotor yokes, which restricts the efficient use of iron, and it is usually avoided by designers [9]. This saturation cannot be predicted by the commonly used one-phase model of SRM. Additionally, extensive finite element analysis of SRM, especially with two phases conducted simultaneously, has revealed the presence of mutual coupling between the stator phases for a large group of candidate designs studied in an optimal design process. So, the modeling of all possible flux paths linking different phases is necessary.

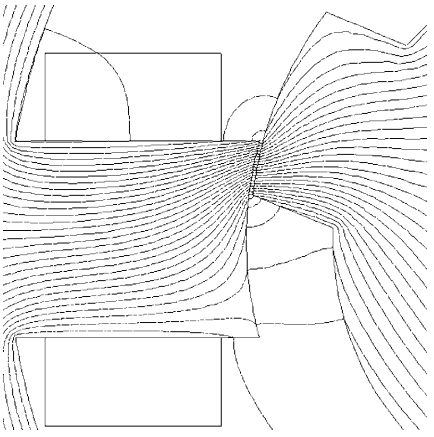

Fig. 1. High levels of saturation and sharp curving of fluxes at corners of partially overlapping stator and rotor poles

The previous attempts in this field do not meet all the requirements mentioned above. In addition, all those which include the effects of mutual coupling and multiphase excitation have no clear reference to the calculation of the machine torque.

This paper describes a general nonlinear magnetic equivalent circuit model of a SRM including all possible flux paths in a 2-D view of the SRM. The model comprises a set of permeance elements linked in series and in parallel and can be applied to the machine with short and full pitched windings. These permeances are mathematically calculated for different parts of the machine based upon the geometries of the flux tubes and, for stator and rotor poles, upon the ratio of the fluxes which are to flow through one common path. A numerical matrix method and an approximate analytic alternative are presented to calculate the total machine torque. Inclusion of the rotor skew in the model is described, and the simulation results are compared with FEM results and measurements.

2 Stator and rotor pole models

To produce useful mechanical torque in SRM, the airgap region conducts the flux lines from the stator poles of the excited phases into the rotor poles and core. As will be described later, this region can be divided into some separate paths so that each one, as a flux tube, conducts a part of the airgap flux. Some of the airgap flux tubes conduct the flux of each stator or rotor pole, which is equal to an algebraic sum of the fluxes flowing through such airgap flux tubes. Moreover, one or more saturable flux tubes can be assumed within the pole to be connected to each of these airgap flux tubes. Assuming one saturable flux tube in the pole connected to each airgap flux tube, its

cross-section area can be determined by the concept of the ratio of fluxes as Eq. (1).

$$a_j = \frac{\varphi_j}{\sum_{k=1}^{n} \varphi_k} A_p \tag{1}$$

where A_p, n, φ_j and a_j ($j = 1, \ldots, n$) are the cross-section area of the stator or rotor pole, the total number of airgap flux tubes which conduct the flux into the pole, the flux value and the cross-section area of the saturable flux tube connected to the jth airgap flux tube, respectively. Therefore, each airgap flux tube which conducts a part of the flux into a stator or rotor pole is connected in the pole to a saturable flux tube whose cross-section area is given by Eq. (1).

But the stator and rotor pole models should be handled more carefully. When a pair of rotor and stator poles exhibit partial overlap, the flux in the overlap region should pass through a small cross-section area within the airgap. While this flux may be insufficient to saturate the whole pole, its density will increase in the airgap near the overlap region. Consequently, it causes high flux densities at the tip of the poles in the overlap region and leads to local saturation phenomena. To deal with local saturation, each airgap flux tube conducting the flux into the pole tip is connected in series to a saturable flux tube whose cross-section area is the same as that of the airgap flux tube. But the length of this saturable flux tube is much smaller than that of the former saturable flux tube defined above.

The stator pole model is divided into two parts, each of them with half of the stator pole length. The first part located near the root of the stator pole is assumed to conduct a homogeneous flux and then modeled with one permeance element. The second part includes a set of permeance elements which are linked in series with airgap permeance elements. Each airgap flux tube conducting the flux into the pole tip is connected in series to two saturable flux tubes in the pole, one with the same cross-section area as the airgap flux tube, but with a short length, and another with the cross-section area given by Eq. (1). Nevertheless, each airgap flux tube conducting the flux into the pole side is connected in the pole only to one saturable flux tube, because the occurrence of local saturation at the pole side is usually improbable. Each of these saturable flux tubes is modeled with one permeance element. The rotor pole model is the same as the second part of the stator pole model. A simple illustration of the model for partially overlapping stator and rotor poles is shown in Fig. 2. As described above, the pole tips are modeled by two series saturable permeance elements, and the pole sides are modeled by one saturable permeance element.

Considering a homogeneous flux distribution within each saturable flux tube, the permeance of the flux tube is calculated by Eq. (2).

$$P = \frac{\mu(B)a}{l} \tag{2}$$

where a, l, $\mu(B)$ and B are the cross-section area, length, permeability and magnetic flux density of the saturable flux tube, respectively. The permeability of the saturable flux tube is a nonlinear function of its magnetic flux density. There are several ways to model this nonlinear

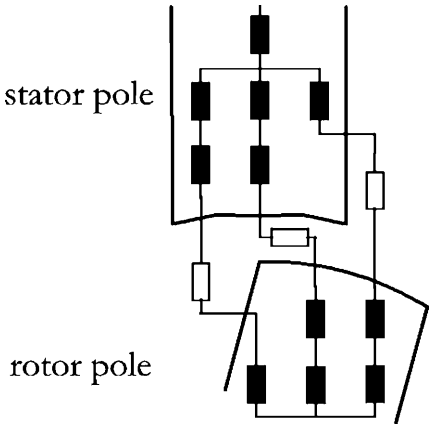

Fig. 2. Lumped model for a pair of stator and rotor poles in a partially overlapping position

quantity. A most straightforward method which gives accurate results is defined in Eq. (3).

$$\mu(B) = \frac{1}{p_1 + p_2|B|^q} \tag{3}$$

where p_1, p_2 and q>0 are constant parameters [9]. These parameters are adjusted in a curve-fitting process to give the best approximation for the nonlinear permeability curve of a selected industrial iron material. However, in this work, the proposed model uses a look-up table of the μ–B curve with a spline interpolation algorithm for calculating the permeability of each saturable flux tube similar to the usual procedure used in commercial FEM software. When the magnetic flux flowing through a flux tube is known, the flux density will be the ratio of the magnetic flux to the average cross-section area of the flux tube, and the permeability is then evaluated by using the look-up table of the μ–B curve. As will be described later, because of this nonlinear dependency, the final equations for the circuit model will be nonlinear. So, the magnetic flux flowing through each saturable flux tube is obtained at each step during an iterative solution of the nonlinear model equations based on the results from the preceding step.

3
Stator and rotor core models

The stator core or yoke has no complexity for modeling, because the flux is distributed nearly homogeneously. Hence, each part of the stator core between two successive stator poles is represented by one permeance element. Later, this permeance element is divided into two identical permeance elements, providing the connection nodes related to the proposed model. In contrast, the rotor core or yoke needs a more subtle model, because it rotates and the flux distribution form changes. In order to find a suitable model, a real flux distribution in a machine with one excited phase is considered at aligned, partially overlapping and unaligned positions of the rotor poles with respect to the excited stator poles, as shown in Fig. 3. Their similar corresponding patterns are conceived as shown in Fig. 4. The angle α is determined by the portion of the flux entering the rotor core under an excited stator pole. The situation is more complicated for multiphase excitation.

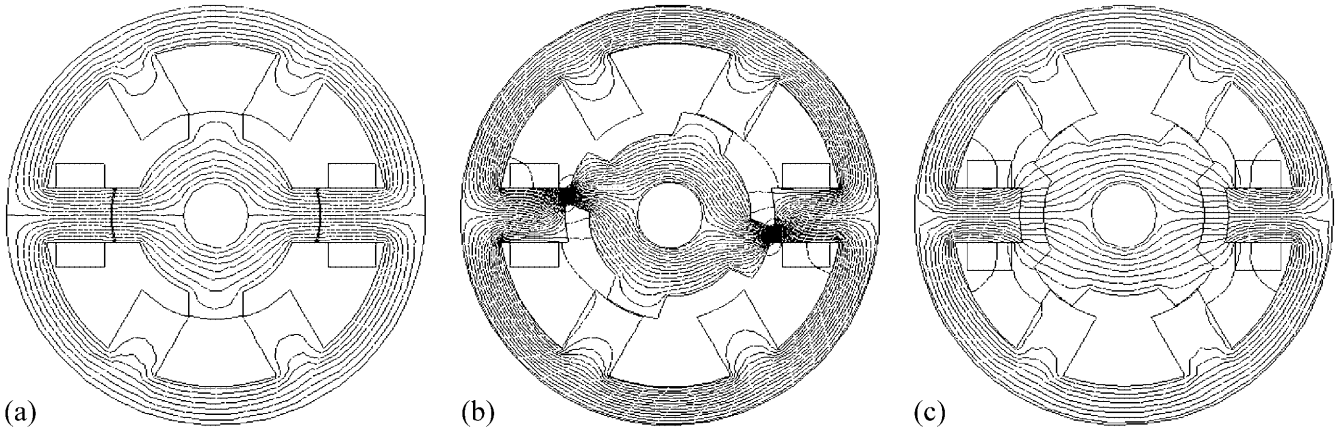

Fig. 3a–c. Flux distributions in stator and rotor poles obtained from FE analysis of SRM for one-phase excitation: **a** aligned position; **b** partially overlapping position; **c** unaligned position

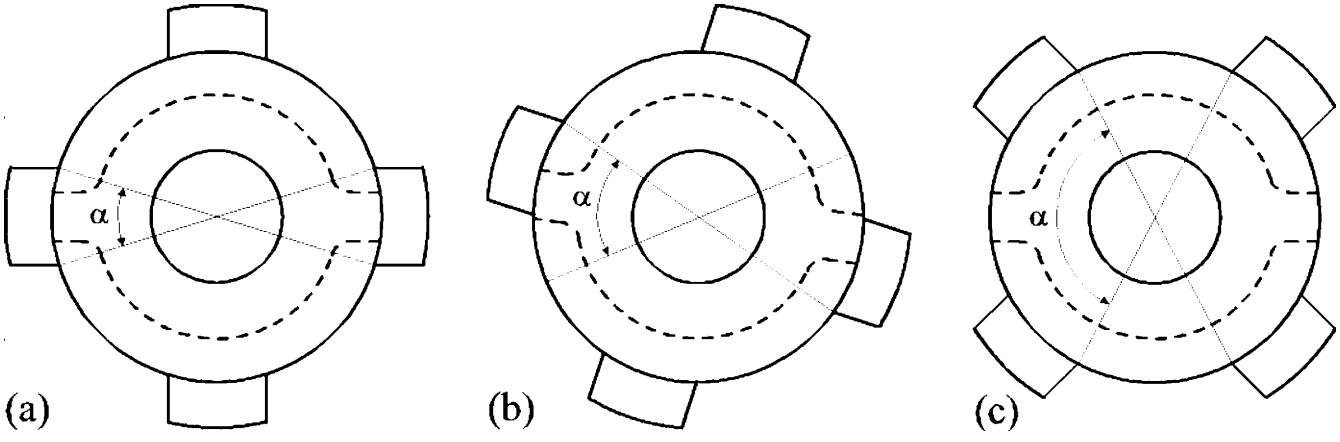

Fig. 4a–c. Flux patterns of the rotor core corresponding to Fig. 3: **a** aligned position; **b** partially overlapping position; **c** unaligned position of stator and rotor poles for one-phase excitation

For simplicity, the angle α under each rotor pole is limited to four values. If there is no airgap path conducting the flux between the rotor pole and the excited stator poles, the angle is taken to be zero. Otherwise, if there are some airgap paths between the rotor pole and the excited stator poles, and there is no airgap path between the rotor yokes at two sides of the rotor pole and excited stator poles, the angle will be β_r. If there are such airgap paths for both of these rotor yokes, the angle will be $2\pi/N_r$. Finally, if there is such an airgap path only for one of the rotor yokes, the angle will be $0.5\beta_r + \pi/N_r$.

Determining the angle α, the pattern of the flux distributed in the segment specified by this angle can show one of the three forms illustrated in Fig. 5. This pattern is dependent upon the direction of the total flux conducted by the rotor pole into this segment and also upon the relative direction of the fluxes in two adjacent rotor poles. A logical set of conditional if-then statements determines the resulting pattern of the flux under each rotor pole. The circuit model of the rotor core is shown in Fig. 6 under two adjacent rotor poles. The permeances under each rotor pole, P_{ur1} and P_{ur2}, are determined by the angle α and the direction of the total fluxes in three nearby rotor poles. One or both of these

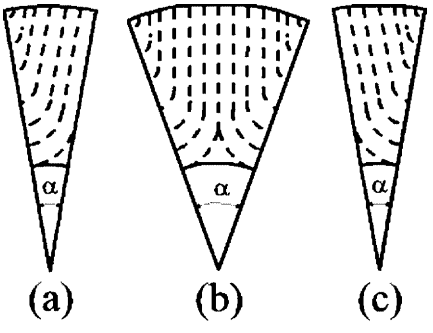

Fig. 5. Flux patterns in the segment specified by angle α under each rotor pole

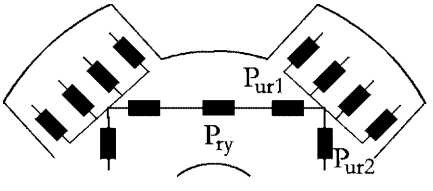

Fig. 6. Rotor core model under two adjacent rotor poles

permeances may disappear. These permeances for pattern (b) in Fig. 5 are determined as following:

$$P_{\text{uri}} = \frac{\mu(B_{\text{uri}})\, l_{\text{stk}}(0.5(r_{\text{rb}} - r_{\text{sh}}) + x)}{\left[\left(\frac{\pi}{2} - 1\right)\frac{r_{\text{sh}}}{r_{\text{rb}}} + \left(1 - \frac{r_{\text{sh}}}{r_{\text{rb}}}\right)\tan^{-1}(0.5\alpha)\right]x + A'} \quad (i = 1, 2) \quad (4)$$

$$A' = r_{\text{rb}}\sqrt{1 - \left(\sin(0.5\alpha) - \frac{x}{r_{\text{rb}}}\right)^2} - r_{\text{rb}}\cos(0.5\alpha) \quad (5)$$

$$x = 0.5 r_{\text{rb}} \sin(0.5\alpha) \quad (6)$$

where $\mu(B_{\text{uri}})$ is a nonlinear function of the magnetic flux density B_{uri}. This flux density is calculated as a ratio of the magnetic flux flowing in the flux tube associated with the permeance element to the average cross-section area of this tube, equal to the denominator of Eq. (4). The permeability is then determined by using the look-up table of the μ–B curve. For the other patterns, one of these permeances disappears and another is determined by Eq. (4) with duplicated x.

The rotor yoke permeance P_{ry} conducts a homogeneous distributed flux and spreads over an angle of $2\pi/N_{\text{r}} - (\alpha_1+\alpha_2)$, where α_1 and α_2 are the aforementioned angles under two adjacent rotor poles at both ends of the yoke.

4 Airgap model

There are two different groups of permeances which are included in the airgap model: leakage and linking. Linking permeances, which fundamentally depend on rotor position, link each stator pole to the rotor poles or core. They are all determined by using the integral form of the flux tube analysis.

$$P = \mu_0 \int \frac{\mathrm{d}a}{l} \quad (7)$$

where da, l and μ_0 are an increment of cross-section area, length and magnetic permeability of the airgap flux tube, respectively. The calculation of airgap permeances depends on the geometric properties of the considered flux tubes and here is handled using the real configuration of the machine parts.

4.1 Airgap leakage permeances

Extensive investigations by FEM analysis of SRM with short and full pitched windings show that there are three different forms of winding slot leakage: pole to core, pole side to pole side, and pole face to pole face leakage. Since the stator slot in a SRM with full pitched winding is generally filled by a side of one phase winding, pole to core leakage does not appear in this case. It is also noted that pole-face to pole-face leakage occurs only when there is no rotor pole between the two stator poles.

4.1.1 Pole to core leakage

Since the leakage path is located in a current carrying region, a simple magnetic formulation is used to include the effect of the source region in the calculation of the permeance. Pole to core leakage paths are modeled by a series of arcs as shown in Fig. 7a. The current in half of the slot is taken to be uniformly distributed. So the current density in this region is given by Eq. (8).

$$J = \frac{4NI}{h_s}\left[\theta_{\text{slot}}\left(r_{\text{sb}} + r_{\text{sp}}\right) + \beta_{\text{s}} h_{\text{s}}\right]^{-1} \quad (8)$$

Assuming that the permeance of the steel is large compared with that of the slot, the magnetic field strength at any given radius r, shown in Fig. 7a, is given by Eq. (9).

$$H_{r,pc} = \frac{Jr}{2}\left(1 + \frac{K_{\text{s}}}{K_{\text{s}} + r}\right) \quad (9)$$

$$K_{\text{s}} = \frac{\beta_s h_{\text{s}}}{(\pi - \beta_{\text{s}})} \quad (10)$$

The leakage flux is assumed to be limited to half of the slot and obtained by integration of the flux density.

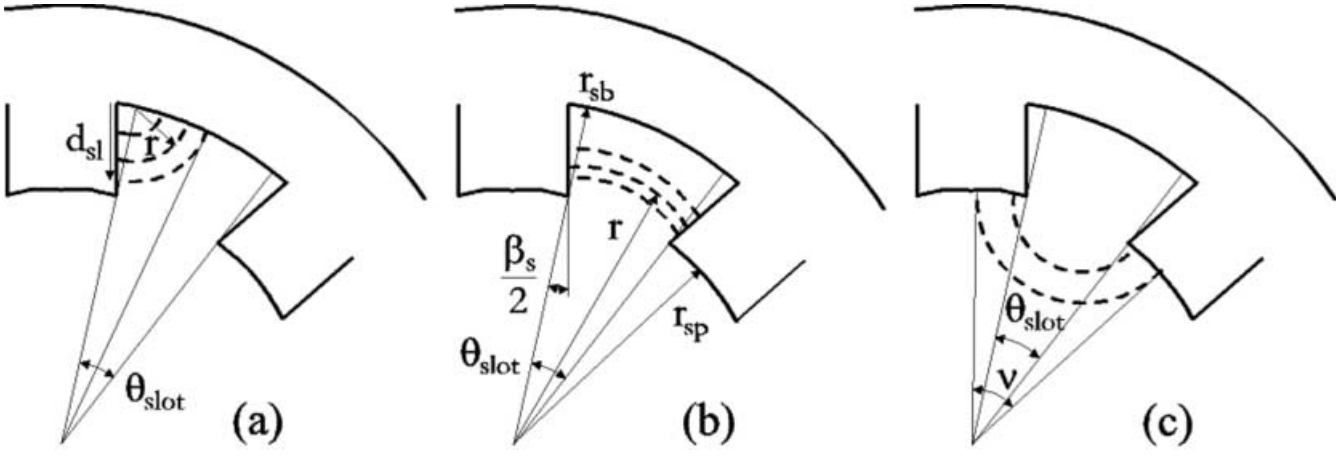

Fig. 7. Airgap paths for **a** pole to core, **b** pole side to pole side, and **c** pole face to pole face leakage permeances

$$\varphi_{pc} = \frac{\mu_0 l_{stk} J}{2}\left[\frac{d_{sl}^2}{2} + K_s d_{sl} - {K_s}^2 \ln\left(\frac{d_{sl}}{K_s} + 1\right)\right] \quad (11)$$

$$d_{sl} = \begin{cases} h_s & 0.5h_s(1 - 0.5\beta_s)/r_{sb} < \sin(0.25\theta_{slot}) \\ 2r_{sb}\sin(0.25\theta_{slot}) + 0.5\beta_s h_s & \text{otherwise} \end{cases} \quad (12)$$

The permeance is then the ratio of total leakage flux to mmf drop.

$$P_{pc} = \frac{\varphi_{pc}}{NI} \quad (13)$$

4.1.2
Pole side to pole side leakage

The path of this leakage flux is modeled by a series of arcs as shown in Fig. 7b. The computation of the related permeance is outlined in different ways for the machines with short and full pitched windings. But the same results are fundamentally obtained for both cases. For the machine with short pitched winding, with the same assumptions as before, the magnetic field strength at any given radius r, shown in Fig. 7b, is determined as follows:

$$H_{r,pp} = \frac{J}{2}(r_{sb} - r)\left(1 + \frac{r_{sb} - K_u}{r - K_u}\right) \quad (14)$$

$$K_u = \frac{\beta_s r_{sp}}{(\theta_{slot} + \beta_s)} \quad (15)$$

From this, the leakage flux can be obtained using Eq. (16) as a function of the arbitrary radius.

$$\varphi^r_{r_{sp}} = \mu_0 l_{stk} J\left[\frac{1}{4}(r_{sp}^2 - r^2) + \frac{K_u}{2}(r - r_{sp} + B')\right] \quad (16)$$

$$B' = \left(K_u + \frac{r_{sb}^2}{K_u} - 2r_{sb}\right)\ln\left(\frac{r - K_u}{r_{sp} - K_u}\right) \quad (17)$$

The permeance of the total path between successive stator poles is then evaluated as a series connection of two of the same permeances associated to two halves of the slot.

$$P_{pp} = \frac{P'_{pp}}{2} = \frac{\varphi^r_{r_{sp}}}{2NI} \quad (18)$$

4.1.3
Pole face to pole face leakage

This leakage flux appears especially during multiphase excitation of the SRM. Modeling of the associated flux path is based on the concept of perpendicular circles as shown in Fig. 7c. So, circles perpendicular to the faces of two successive stator poles are considered. The radius and arc length of such circles corresponding to angle v are determined by Eqs. (19) and (20).

$$r_v = r_{sp}\tan(0.5v) \quad (19)$$

$$l_v = r_{sp}(\pi - v)\tan(0.5v) \quad (20)$$

Assuming that the leakage flux is restricted to half the pole face, the average leakage permeance is given by Eq. (21).

$$P_{ff} = \mu_0 l_{stk}\beta_s\left[C' + \left(\pi - \frac{2\pi}{N_s}\right)\tan\left(\frac{\pi}{N_s}\right)\right] \quad (21)$$

$$C' = \left(\pi - \frac{2\pi}{N_s} + \beta_s\right)\tan\left(\frac{\pi}{N_s} - \frac{\beta_s}{2}\right) \quad (22)$$

4.2
Airgap linking permeances

These permeances, which play a major role in determining the performance of the SRM, are modeled based on three regions defined in Fig. 8. This figure shows an ideal piecewise linear inductance of one phase versus rotor angular position. The phase inductance is maximum in the aligned position of stator and rotor poles and minimum in the unaligned position. The important boundary angles between these regions are determined by Eqs. (23) and (24).

$$\xi_1 = 0.5(\beta_r - \beta_s) \quad (23)$$

$$\xi_2 = 0.5(\beta_r + \beta_s) \quad (24)$$

There are five different permeances which comprise all linking flux paths between stator and rotor: overlap, stator pole side to rotor pole face, stator pole face to rotor pole side, stator pole face to rotor core, and stator pole side to rotor pole side. The graphical modeling of the airgap paths corresponding to these permeances is shown in Figs. 9–11 for the three mentioned regions. An important assumption observed throughout the modeling is that the total linking flux from the face of an excited stator pole to a rotor pole segment is restricted to the intersection of the rotor interpolar axis and the stator pole face. Here, the rotor pole segment is defined as a part of the rotor which is constricted by two successive rotor interpolar axes. In other words, while the rotor interpolar axis has not crossed the stator pole face, there is only one rotor pole that can be linked to the stator pole face. This most useful hypothesis guarantees the symmetry of the airgap modeling in the

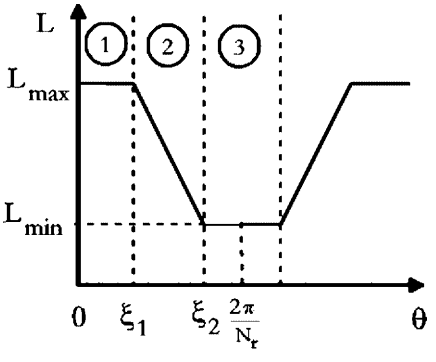

Fig. 8. Ideal trapezoidal variations of phase inductance and three defined regions

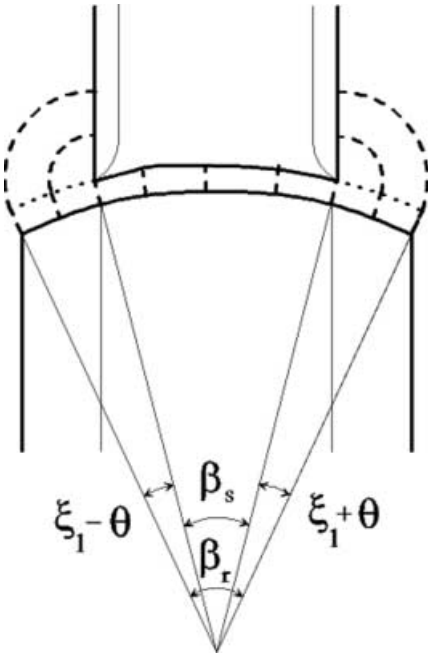

Fig. 9. Graphical modeling of airgap paths for region 1

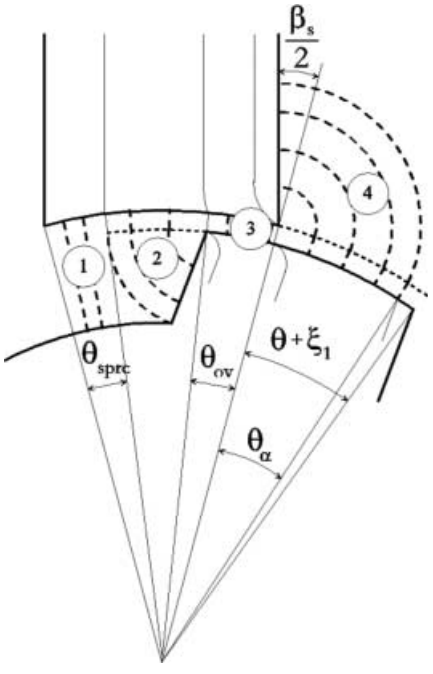

Fig. 10. Graphical modeling of airgap paths for region 2

fully unaligned position of a stator pole. Figure 11 shows only the linking permeances between the stator pole and one nearby rotor pole. It is evident that there is also a linking flux between the stator pole and another nearby rotor pole, because the rotor interpolar axis intersects the stator pole face. Upon the above assumption, four states can be generally considered for partially overlapping stator and rotor poles (region 2) during rotor rotation. The occurrence of each state is dependent upon the geometric properties of the machine. These states are

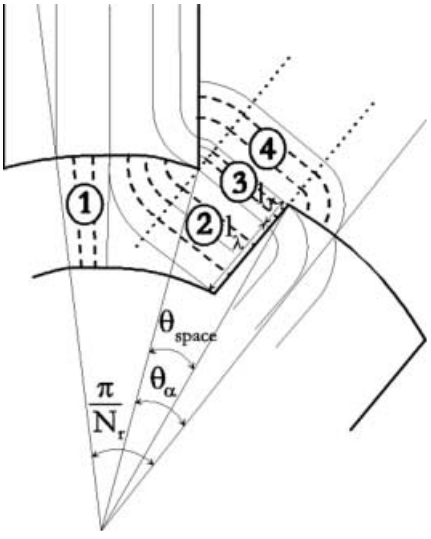

Fig. 11. Graphical modeling of airgap paths for region 3

defined as follows, based on airgap paths 1 and 2 shown in Fig. 10.

1. There is only the airgap path 2, and the rotor interpolar axis does not cross the stator pole face.
2. There is only the airgap path 2, and the rotor interpolar axis crosses the stator pole face.
3. There are both airgap paths 1 and 2, and the rotor interpolar axis does not cross the stator pole face.
4. There are both airgap paths 1 and 2, and the rotor interpolar axis crosses the stator pole face.

For non-overlapping stator and rotor poles (region 3), six states are considered of which four states are identical to the states defined above, but for the airgap paths shown in Fig. 11. The two extra states are defined as follows.

5. There is only the airgap path 1, and the rotor interpolar axis does not cross the stator pole face.
6. There is only the airgap path 1, and the rotor interpolar axis crosses the stator pole face.

4.2.1 Overlap permeance

The overlap permeance occurs directly between rotor and stator poles in the narrow region of the overlap. This permeance is given by Eqs. (25) and (26).

$$P_{ov} = 0.5\mu_0 l_{stk}(r_{sp} + r_{rp})\theta_{ov}/g \tag{25}$$

$$\theta_{ov} = \begin{cases} \beta_s & 0 \le |\theta| \le \xi_1 \\ \xi_2 - |\theta| & \xi_1 < |\theta| \le \xi_2 \\ 0 & \xi_2 < |\theta| \end{cases} \tag{26}$$

The fringing effects for the aligned corners of the stator and rotor poles are considered by introducing an average fringing permeance which is in parallel with the overlap permeance and given by Eq. (27). The fringing flux tubes are assumed to be several semicircles extended to a very small cross section of the airgap.

$$P_{fr} = \frac{2\mu_0 l_{stk}}{\pi} \tag{27}$$

4.2.2
Stator pole side to rotor pole face permeance

The flux tube, linking a stator pole side to a rotor pole face, is modeled by two different shapes for overlapping and non-overlapping stator and rotor poles, as shown in Figs. 9–11. For overlapping stator and rotor poles, the permeance is determined by Eq. (28).

$$P_{\text{ssrp}} = \frac{\mu_0 l_{\text{stk}}}{0.5\pi + \theta_\alpha} \ln\left[1 + r_{\text{rp}}(0.5\pi + \theta_\alpha)\theta_\alpha/(g)\right] \tag{28}$$

where θ_α is shown in Fig. 10. The flux flowing through this permeance is assumed to be restricted either to the upper half of the stator pole side or to half of the stator slot angle. Upon this assumption, θ_α may be restricted to one of the following angles, whichever is smaller.

$$\theta_5 = \frac{h_{\text{s}}}{2r_{\text{rp}}} \tag{29}$$

$$\theta_6 = \frac{\pi}{N_{\text{s}}} - \frac{\beta_{\text{s}}}{2} \tag{30}$$

For non-overlapping stator and rotor poles, the permeance is calculated by Eq. (31).

$$P_{\text{ssrp}} = \frac{\mu_0 l_{\text{stk}}}{(0.5\pi + \theta_\alpha)} \times \ln[1 + (0.5\pi + \theta_\alpha)(\lambda_{\max} - \lambda_\theta)/(g + \lambda_\theta \cdot \theta + \omega_\theta)] \tag{31}$$

where $\lambda_{\max}$ is given by Eq. (32).

$$\lambda_{\max} = \begin{cases} r_{\text{rp}}\beta_{\text{r}} + \lambda_\theta & \theta_\alpha < \theta_5 \& \theta_\alpha < \theta_6 \\ r_{\text{rp}}\theta_5 & \theta_\alpha \geq \theta_5 \& \theta_5 < \theta_6 \\ r_{\text{rp}}(\theta_6 - \theta_{\text{space}}) + \lambda_\theta & \theta_\alpha \geq \theta_6 \& \theta_6 < \theta_5 \end{cases} \tag{32}$$

$$\theta_{\text{space}} = \theta - \xi_2 \tag{33}$$

Ignoring the small airgap length for non-overlapping stator and rotor poles, three important parameters are defined by Eqs. (34)–(36), as shown in Fig. 12.

$$\lambda_\theta = r_{\text{rp}}[\cos 0.5\beta_{\text{r}} - \cos(\theta - 0.5\beta_{\text{s}})] \tag{34}$$

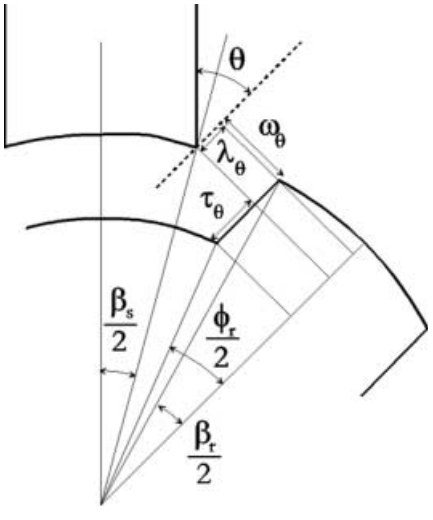

Fig. 12. Graphical definition of some parameters for region 3

$$\omega_\theta = r_{\text{rp}}[\sin(\theta - 0.5\beta_{\text{s}}) - \sin 0.5\beta_{\text{r}}] \tag{35}$$

$$\tau_\theta = r_{\text{rp}}[\cos(\theta - 0.5\beta_{\text{s}}) - \tau_{\text{r}}] \tag{36}$$

$$\tau_{\text{r}} = \sqrt{(r_{\text{rb}}/r_{\text{rp}})^2 - \sin^2(0.5\beta_{\text{r}})} \tag{37}$$

This permeance disappears at an angle called θ_7, when $\lambda_{\max} = \lambda_\theta$.

4.2.3
Stator pole face to rotor pole side permeance

This permeance is identified by the airgap path 2 in Figs. 10 and 11. This airgap path is modeled using a series of arcs and straight lines. The arcs correspond to an angle of $\pi/2+\xi_1-\theta$. The straight lines are perpendicular to the rotor pole side. The permeance is given by Eq. (38) for overlapping stator and rotor poles.

$$P_{\text{sprs}} = \frac{\mu_0 l_{\text{stk}}}{0.5\pi + \xi_1 - \theta} \ln\left[1 + r_{\text{rp}}(\theta - \xi_1 - \theta_0)(0.5\pi + \xi_1 - \theta)/g\right] \tag{38}$$

$$\theta_0 = \begin{cases} 0 & (\text{state} : 1) \\ \theta - \theta_2 & (\text{state} : 2) \\ \theta - \xi_1 - (h_{\text{r}}/r_{\text{rp}}) & (\text{state} : 3 \,\&\, 4) \end{cases} \tag{39}$$

$$\theta_2 = \frac{\pi}{N_{\text{r}}} - \frac{\beta_{\text{s}}}{2} \tag{40}$$

where θ_2 is a relative angle between the stator and rotor poles at which the rotor interpolar axis touches the corner of the stator pole face. The permeance is given by Eq. (41) for non-overlapping poles, as shown in Fig. 11.

$$P_{\text{sprs}} = \frac{\mu_0 l_{\text{stk}}}{0.5\pi + \xi_1 - \theta} \ln\left[1 + r_{\text{rp}}(\beta_{\text{s}} - \theta_0')(0.5\pi + \xi_1 - \theta)/(g + \omega_\theta)\right] \tag{41}$$

$$\theta_0' = \begin{cases} 0 & (\text{state} : 1) \\ \theta - \theta_2 & (\text{state} : 2) \\ \beta_{\text{s}} - (\tau_\theta/r_{\text{rp}}) & (\text{state} : 3 \,\&\, 4) \\ \beta_{\text{s}} & (\text{state} : 5 \,\&\, 6) \end{cases} \tag{42}$$

This permeance disappears, when the relative angle between the stator and rotor poles is greater than one of the two following angles, whichever is smaller.

$$\theta_4 = 0.5\beta_{\text{s}} + \cos^{-1}(\tau_{\text{r}}) \tag{43}$$

$$\theta_8 = \frac{\pi}{N_{\text{r}}} + \frac{\beta_{\text{s}}}{2} \tag{44}$$

The angle θ_4 corresponds to a condition that τ_θ is equal to zero. The angle θ_8 corresponds to a condition that the rotor interpolar axis touches the next corner of the stator pole face. These conditions fundamentally result from the presence and absence of airgap path 1 respectively.

4.2.4
Stator pole face to rotor core permeance

This permeance which has not been considered in previous work, plays an important role in determining the flux distribution in the unaligned and non-overlapping

positions (region 3). The flux tube associated with this permeance conducts the radial flux lines. The permeance is simply determined by Eq. (45).

$$P_{\text{sprc}} = \frac{\mu_0 l_{\text{stk}}}{2(r_{\text{sp}} - r_{\text{rb}})}(r_{\text{sp}} + r_{\text{rb}})\theta_{\text{sprc}} \tag{45}$$

where θ_{sprc} for overlapping stator and rotor poles is:

$$\theta_{\text{sprc}} = \begin{cases} 0 & (\text{state} : 1\&2) \\ \theta - \xi_1 - (h_{\text{r}}/r_{\text{rp}}) & (\text{state} : 3) \\ \theta_8 - \xi_2 - (h_{\text{r}}/r_{\text{rp}}) & (\text{state} : 4) \end{cases} \tag{46}$$

and for non-overlapping poles is:

$$\theta_{\text{sprc}} = \begin{cases} 0 & (\text{state} : 1\&2) \\ \beta_{\text{s}} - (\tau_\theta/r_{\text{rp}}) & (\text{state} : 3) \\ \theta_8 - \theta - (\tau_\theta/r_{\text{rp}}) & (\text{state} : 4) \\ \beta_{\text{s}} & (\text{state} : 5) \\ \theta_8 - \theta & (\text{state} : 6) \end{cases} \tag{47}$$

4.2.5
Stator pole side to rotor pole side permeance

The flux flowing between stator and rotor pole sides is observed in the unaligned and non-overlapping positions of the stator and rotor poles for the most SRMs analyzed by FEM. This flux path is not clearly addressed by other authors. The associated permeance is calculated based upon the three defined parameters in Eqs. (34)–(36) and the shape of the flux tube illustrated in Fig. 11. While this airgap path is not constricted by the end of the rotor pole side at the root of the rotor pole, the permeance is given by Eq. (48).

$$P_{\text{ssrs}} = \frac{\mu_0 l_{\text{stk}}}{\theta} \ln\left(1 + \frac{l\gamma}{g + \omega_\theta}\theta\right) \tag{48}$$

$$l\gamma = \begin{cases} \lambda_\theta & (\theta \le \theta_7) \\ \lambda_{\max} & (\theta > \theta_7) \end{cases} \tag{49}$$

Otherwise, when the end of the rotor pole side at the root of the rotor pole restricts this flux path, the permeance is given by Eq. (50). This condition occurs only when the airgap path 2 has already disappeared.

$$P_{\text{ssrs}} = \frac{\mu_0 l_{\text{stk}}}{\theta} \ln\left[1 + \frac{l_\gamma}{g + \omega_\theta + (\lambda_\theta - h_{\text{r}})\theta}\theta\right] \tag{50}$$

$$l\gamma = \begin{cases} h_{\text{r}} & (\theta \le \theta_7) \\ \lambda_{\max} + h_{\text{r}} - \lambda_\theta & (\theta > \theta_7) \end{cases} \tag{51}$$

This permeance disappears at an angle called θ_9, when $\lambda_\theta = \lambda_{\max} + h_{\text{r}}$.

5
Complete model and solution

For a SRM with N_{s} stator poles and N_{r} rotor poles, the complete magnetic equivalent circuit model includes several sub-circuits such as those shown in Fig. 13. For simplicity, the airgap linking permeances have been shown by dashed lines, and the airgap leakage permeances as well as the saturable iron permeances have been emphasized. For the SRM with full pitched winding, magneto motive force (mmf) sources have been proposed by [10] in series with stator yoke permeances. In this machine, the flux is

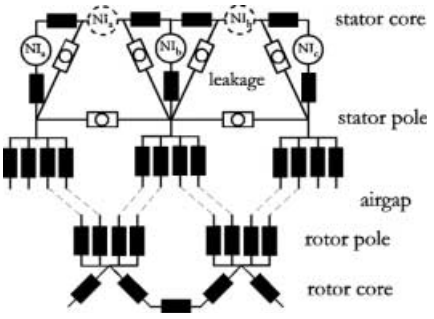

Fig. 13. Sub-circuit of the proposed magnetic equivalent circuit model

directed through each stator pole by two phases, unlike the machine with short pitched winding in which only one phase directs the flux through an excited stator pole. Therefore, there are two different mmf sources in the sub-circuit: one in series with the stator yoke for SRM with full pitched winding and another in series with the stator pole for the machine with short pitched winding. For each case, only the appropriate mmf sources are then used, and the other mmf sources are taken to be zero. In addition, for the machine with full pitched winding, pole to core leakage permeances vanish. The existence of the airgap linking permeances between each pair of stator and rotor poles is dependent on their relative position. While the relative angle between their axes is greater than θ_9, there will be no airgap path between them. Otherwise, the permeances of stator pole tip, rotor pole and linking airgap for each airgap path are determined and combined. Then, the resulting permeances for parallel airgap paths are merged together to make a single permeance in the circuit model, representing the existent flux path between a pair of stator and rotor poles.

The complete circuit may be solved by node, mesh or other circuit analysis methods. To simplify formulae in the next sections, the mesh method is selected. The resulting matrix equation is then given by:

$$[\mathbf{Z}][\mathbf{\Phi}] = [\mathbf{F}] \tag{52}$$

where **Z**, **Φ**, and **F** are impedance or reluctance matrix, mesh flux vector, and mmf source matrix, respectively. The elements of the reluctance matrix comprise some series and parallel combinations of the airgap and saturable permeances. Each saturable iron permeance is nonlinearly dependent on the magnetic flux flowing through its corresponding flux tube. This magnetic flux can be represented by a combination of the mesh fluxes. So the elements of the reluctance matrix are nonlinearly dependent on the mesh fluxes. In other words, **Z** is a nonlinear function of **Φ** in Eq. (52), and the resulting matrix equation will be nonlinear. Therefore, it should be solved using an iterative method such as Gauss–Seidel or Newton–Raphson. The Newton–Raphson method requires calculation of the Jacobian matrix whose elements will be functions of partial differentials of the permeances with respect to the mesh fluxes. Since the permeances are not the explicit functions of the mesh fluxes, the analytic derivative is not possible and a numerical derivative should be used. However, this can adversely affect the accuracy of the re-

sults. Therefore, a Gauss–Seidel method is used to solve Eq. (52). The solution process begins with an initial flat permeability for iron parts and zero values for the angles α under all rotor poles. Then, all airgap and saturable permeances are calculated, and Eq. (52) is solved. The branch fluxes are determined from the resulting mesh fluxes and the values of the saturable permeances calculated at the last step. Then, the cross-section areas of the flux tubes corresponding to the stator and rotor pole tips using Eq. (1), the new values of the angles α, and the new values of the permeances are calculated, and Eq. (52) is solved. This iterative process is repeatedly executed to reach an acceptable error between the successive solutions of the mesh fluxes.

Assuming that the stator poles of the excited phase participate in mesh-loops 1, 2, k and k+1, the magnetic flux in each of these poles is given by:

$$\psi_1 = \varphi_1 - \varphi_2 = \varphi_k - \varphi_{k+1} \tag{55}$$

In this case, one can write $\mathbf{F} = \mathbf{E}Ni_1$ where:

$$[\mathbf{E}] = [1 \quad -1 \quad 0 \quad \cdots \quad 0 \quad 1 \quad -1 \quad 0 \quad \cdots \quad 0]^{\mathrm{T}} \tag{56}$$

Adding the first equation to the second and (k+1)th equations of Eq. (52), and subtracting it from the kth equation, vector $\mathbf{E}$ is converted to a vector which has only one non-zero element in the first row. Replacing φ_1 in terms of ψ_1 from Eq. (55), Eq. (52) can be formed as:

$$\begin{bmatrix} z_{11} & z_{12}+z_{11} & z_{13} & \cdots \\ z_{21}+z_{11} & z_{22}+z_{12}+z_{21}+z_{11} & z_{23}+z_{13} & \cdots \\ \vdots & \vdots & \vdots & \\ z_{k1}-z_{11} & z_{k2}-z_{12}+z_{k1}-z_{11} & z_{k3}-z_{13} & \cdots \\ z_{(k+1)1}+z_{11} & z_{(k+1)2}+z_{12}+z_{(k+1)1}+z_{11} & z_{(k+1)3}+z_{13} & \cdots \\ \vdots & \vdots & \vdots & \end{bmatrix} \begin{bmatrix} \psi_1 \\ \varphi_2 \\ \vdots \\ \varphi_k \\ \varphi_{k+1} \\ \vdots \end{bmatrix} = \begin{bmatrix} 1 \\ 0 \\ \vdots \\ 0 \\ 0 \\ \vdots \end{bmatrix} Ni_1 \tag{57}$$

6 Dynamic analysis

For the dynamic analysis, the flux linkage of each phase Ψ_i ($i = 1, ..., N_{\mathrm{ph}}$) is given by:

$$\Psi_i = N\psi_i = \int_0^t (V - Ri_i)dt \tag{53}$$

where Ψ_i, V, R and N_{ph} are the magnetic flux in each stator pole excited by the ith phase, the applied voltage to each phase, the phase resistance and the number of machine phases, respectively. The discrete form of Eq. (53) is given by Eq. (54):

$$\Psi_i = \Psi_{i0} + (V - Ri_{i0})(\Delta\theta/\omega_m) \tag{54}$$

where ω_{m} and $\Delta\theta$ are respectively the rotor angular speed and an increment of the rotor angle, and the subscript 0 denotes the values of the quantities from the preceding step. The flux linkage of each phase is determined using Eq. (54) at each step of rotation based on the values of the phase current and flux linkage at the last step. So, the flux linkage of each phase is known from Eq. (54) at each step during the dynamic analysis, and the current of each phase should be calculated by using the machine model. This is completely opposed to the procedure used to determine the static magnetization curves where the phase current is known as a predefined value, and the flux linkage of the phase winding should be calculated by using the machine model. The form of Eq. (52) is much more suitable for the latter procedure than for the former one. Because the mmf matrix $\mathbf{F}$ is known for the latter procedure, Eq. (52) will be a classical nonlinear matrix equation. But for the former procedure, some mesh fluxes and all mmf sources are unknown. So, Eq. (52) should be somewhat manipulated to be solved for the phase currents. For simplicity, one-phase excitation of the SRM is considered initially.

or

$$\begin{bmatrix} \mathbf{R}_{11} & \mathbf{R}_{12} \\ \mathbf{R}_{21} & \mathbf{R}_{22} \end{bmatrix} \begin{bmatrix} \psi_1 \\ \mathbf{\Phi}' \end{bmatrix} = \begin{bmatrix} 1 \\ \mathbf{0} \end{bmatrix} Ni_1 \tag{58}$$

Given the value of Ψ_1, Φ' is obtained from solving Eq. (58) by the same iterative method as mentioned for Eq. (52).

$$\mathbf{R}_{22}\Phi' = -\mathbf{R}_{21}\boldsymbol{\psi}_1 \tag{59}$$

Then,

$$Ni_1 = \mathbf{R}_{11}\boldsymbol{\psi}_1 + \mathbf{R}_{12}\Phi' \tag{60}$$

Similarly, this procedure can be applied to multiphase excitation. For example, in the case of two-phase excitation, the final matrix equation is given by:

$$\begin{bmatrix} \mathbf{R}_{11} & 0 & \mathbf{R}_{13} \\ 0 & \mathbf{R}_{22} & \mathbf{R}_{23} \\ \mathbf{R}_{31} & \mathbf{R}_{32} & \mathbf{R}_{33} \end{bmatrix} \begin{bmatrix} \psi_1 \\ \psi_2 \\ \Phi' \end{bmatrix} = \begin{bmatrix} 1 & 0 \\ 0 & 1 \\ \mathbf{0} & \mathbf{0} \end{bmatrix} \begin{bmatrix} Ni_1 \\ Ni_2 \end{bmatrix} \tag{61}$$

or

$$\mathbf{R}_{33}\Phi' = -\mathbf{R}_{31}\psi_1 - \mathbf{R}_{32}\boldsymbol{\psi}_2 \tag{62}$$

$$Ni_1 = \mathbf{R}_{11}\boldsymbol{\psi}_1 + \mathbf{R}_{13}\Phi' \tag{63}$$

$$Ni_2 = \mathbf{R}_{22}\boldsymbol{\psi}_2 + \mathbf{R}_{23}\Phi' \tag{64}$$

It should be noted that because of the special configuration of the proposed circuit model, any mesh cannot include two or more mmf sources. So, Φ' is obtained from solving Eq. (62), and then i_1 and i_2 are readily calculated by using Eqs. (63) and (64).

7 Calculation of torque

Assuming initially one-phase excitation, the co-energy W_{c} at a given rotor position is defined by Eq. (65).

$$W_c = \int_0^{i_1} \Psi_1(\theta, i')\mathrm{d}i'_1 = \int_0^{Ni_1} \psi_1(\theta, i'_1)\mathrm{d}(Ni'_1) \qquad (65)$$

where the prime denotes the variable of the integration. This integration is equal to the area under the nonlinear curve of $\psi_1(Ni_1)$ at a given rotor position. This curve, which is fundamentally the static magnetization curve of one phase of the machine corresponding to the given rotor position, cannot be formed as an analytic function. So, the integration in Eq. (65) is numerically approximated. If $\Delta f = Ni_1/m$ is the width of the stripes for the discrete integration and ψ_{1j} ($j = 1, ..., m$) is the flux value of the excited stator pole obtained by solving Eq. (52) for $j\Delta f$ as the mmf source corresponding to the excited phase, then the co-energy is approximated by:

$$W_c = \left(\sum_{j=1}^{m} \psi_{1j} - 0.5\psi_{1m}\right)\Delta f \qquad (66)$$

A graphical illustration of this approximation is shown in Fig. 14. Evidently, the accuracy of the evaluated co-energy in Eq. (66) is dependent upon the value of m so that the greater values of m yield the better approximations of the continuous integration in Eq. (65). Calculating this quantity for two very close positions of the rotor with the same phase current, the torque is given by Eq. (67).

$$T(\theta, i_1) = -\frac{\partial W_c(\theta, i_1)}{\partial \theta} = \frac{W_c(\theta, i_1) - W_c(\theta + \Delta\theta, i_1)}{\Delta\theta} \qquad (67)$$

A similar procedure can be used to evaluate the torque by using the stored energy. In this case, the required points of the nonlinear curve of $Ni_1(\psi_1)$ for a discrete integration should be calculated by using a procedure as explained for dynamic analysis. Because the value of the flux for each point of the curve is known, the corresponding mmf value of the excited phase should be determined. However, the numerical method need $2m$ times the solution of Eq. (52), and it can be very time consuming.

A corresponding analytic approach can be derived by using Eq. (58) and the concept of the stored energy as follows:

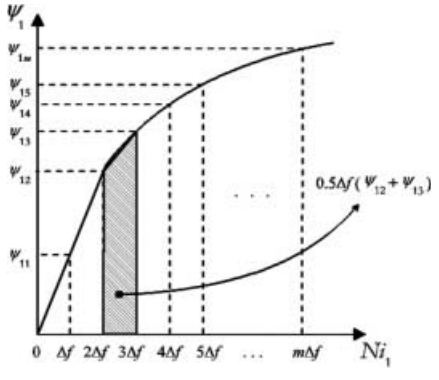

Fig. 14. Graphical illustration of discrete integration for approximating the co-energy

$$W_f = \int_0^{\Psi_1} i_1 \mathrm{d}\Psi_1 = \int_0^{\psi_1} (Ni_1)\mathrm{d}\psi_1 = \int_0^{\psi_1} \left(\mathbf{R}_{11} - \mathbf{R}_{12}\mathbf{R}_{22}^{-1}\mathbf{R}_{21}\right)\psi_1 \mathrm{d}\psi_1 = 0.5\left(\mathbf{R}_{11} - \mathbf{R}_{12}\mathbf{R}_{22}^{-1}\mathbf{R}_{21}\right)\psi_1^2 \qquad (68)$$

$$T(\theta, \psi_1) = \frac{\partial W_f(\theta, \psi_1)}{\partial \theta} = 0.5\psi_1^2 \frac{\partial\left(\mathbf{R}_{11} - \mathbf{R}_{12}\mathbf{R}_{22}^{-1}\mathbf{R}_{21}\right)}{\partial \theta} \qquad (69)$$

Since $\mathbf{R}_{11}$, $\mathbf{R}_{12}$ and $\mathbf{R}_{21}$ are fundamentally no functions of θ, then:

$$T(\theta, \psi_1) = -0.5\psi_1^2 \frac{\partial \mathbf{R}_{22}^{-1}}{\partial \theta} = 0.5\psi_1^2 \mathbf{R}_{22} \frac{\partial \mathbf{R}_{22}}{\partial} \mathbf{R}_{22} \qquad (70)$$

using:

$$\frac{\partial}{\partial \theta}\left(\mathbf{R}_{22}\mathbf{R}_{22}^{-1}\right) = \frac{\partial}{\partial \theta}(\mathbf{I}_e) = \mathbf{0} \qquad (71)$$

This analytic approach assumes that $\mathbf{R}_{ij}$ ($i = 1, 2$ & $j = 1, 2$) obtained from solving Eq. (58) for the flux value of ψ_1 is constant during the calculation of the integration in Eq. (68). This assumption is correct for a linear static magnetization curve, where $\mathbf{R}_{ij}$ is no function of ψ_1 (or i_1). Consequently, this approach gives more acceptable results for the machines with low levels of saturation [8].

For two-phase excitation, the co-energy at a given rotor position is calculated in steps as follows.

$$\begin{aligned} W_c(\theta, i_1, i_2) &= \int_0^{i_1} \Psi_1(\theta, i'_1, i'_2 = 0)\mathrm{d}i'_1 \\ &\quad + \int_0^{i_2} \Psi_2\left(\theta, i'_1 = i_1, i'_2\right)\mathrm{d}i'_2 \\ &= \int_0^{Ni_1} \psi_1(\theta, Ni'_1, Ni'_2 = 0)\mathrm{d}(Ni'_1) \\ &\quad + \int_0^{Ni_2} \psi_2(\theta, Ni'_1 = Ni_1, Ni'_2)\mathrm{d}(Ni'_2) \end{aligned} \qquad (72)$$

The two last integrals can be numerically calculated like Eq. (66). For this purpose, Eq. (52) is solved m times with $j\Delta f_1$ ($j = 1, ..., m$) as the mmf source of phase 1 and zero as the mmf source of phase 2, where $\Delta f_1 = Ni_1/m$, in order to calculate the first integral in Eq. (72). Then, it is solved again m times with Ni_1 as the mmf source of phase 1 and $j\Delta f_2$ ($j = 1, ..., m$) as the mmf source of phase 2, where $\Delta f_2 = Ni_2/m$, in order to calculate the second integral in Eq. (72). The nonlinear curve of $\Psi_2(\theta, Ni'_1 = Ni_1, Ni'_2)$ is the static magnetization curve of phase 2 at a given rotor position of θ, when phase 1 is excited by a constant current level of i_1. The torque is then evaluated like Eq. (67).

$$T(\theta, i_1, i_2) = -\frac{\partial W_c(\theta, i_1, i_2)}{\partial \theta} = \frac{W_c(\theta, i_1, i_2) - W_c(\theta + \Delta\theta, i_1, i_2)}{\Delta\theta} \qquad (73)$$

The analytic approach for calculating the torque can be derived in a similar way to one-phase excitation using the stored energy. The stored energy at a given rotor position is calculated in steps as:

$$\begin{aligned} W_f(\theta,\psi_1,\psi_2) &= \int_0^{\psi_1} Ni_1\big(\theta,\psi_1',\psi_2'=0\big)\mathrm{d}\psi_1' \\ &\quad + \int_0^{\psi_2} Ni_2\big(\theta,\psi_1'=\psi_1,\psi_2'\big)\mathrm{d}\psi_2' \\ &= \int_0^{\psi_1} \big(\mathbf{R}_{11}'' - \mathbf{R}_{12}''\mathbf{R}_{22}''^{-1}\mathbf{R}_{21}''\big)\psi_1'\mathrm{d}\psi_1' \\ &\quad + \int_0^{\psi_2} \big[-\mathbf{R}_{23}'''\mathbf{R}_{33}'''^{-1}\mathbf{R}_{31}'''\psi_1 \\ &\quad + \big(\mathbf{R}_{22}''' - \mathbf{R}_{23}'''\mathbf{R}_{33}'''^{-1}\mathbf{R}_{32}'''\big)\psi_2'\big]\mathrm{d}\psi_2' \\ &= 0.5\big(\mathbf{R}_{11}'' - \mathbf{R}_{12}''\mathbf{R}_{22}''^{-1}\mathbf{R}_{21}''\big)\psi_1^2 \\ &\quad - \mathbf{R}_{23}'''\mathbf{R}_{33}'''^{-1}\mathbf{R}_{31}'''\psi_1\psi_2 \\ &\quad + 0.5\big(\mathbf{R}_{22}''' - \mathbf{R}_{23}'''\mathbf{R}_{33}'''^{-1}\mathbf{R}_{32}'''\big)\psi_2^2 \end{aligned} \tag{74}$$

where $\mathbf{R}_{ij}''$ ($i=1,2$ & $j=1,2$) and $\mathbf{R}_{ij}'''$ ($i=1,2,3$ & $j=1,2,3$) are obtained from the solution of Eq. (75) and Eq. (76), respectively.

$$\begin{bmatrix} \mathbf{R}_{11}'' & \mathbf{R}_{12}'' \\ \mathbf{R}_{21}'' & \mathbf{R}_{22}'' \end{bmatrix} \begin{bmatrix} \psi_1 \\ \Phi' \end{bmatrix} = \begin{bmatrix} 1 \\ \mathbf{0} \end{bmatrix} Ni_1 \tag{75}$$

$$\begin{bmatrix} \mathbf{R}_{11}''' & 0 & \mathbf{R}_{13}''' \\ 0 & \mathbf{R}_{22}''' & \mathbf{R}_{23}''' \\ \mathbf{R}_{31}''' & \mathbf{R}_{32}''' & \mathbf{R}_{33}''' \end{bmatrix} \begin{bmatrix} \psi_1 \\ \psi_2 \\ \Phi' \end{bmatrix} = \begin{bmatrix} 1 & 0 \\ 0 & 1 \\ \mathbf{0} & \mathbf{0} \end{bmatrix} \begin{bmatrix} Ni_1 \\ Ni_2 \end{bmatrix} \tag{76}$$

Since only $\mathbf{R}_{22}''$ and $\mathbf{R}_{33}'''$ are functions of θ, the torque is given by Eq. (77).

$$\begin{aligned} T(\theta,\psi_1,\psi_2) &= \frac{\partial W_f(\theta,\psi_1,\psi_2)}{\partial\theta} = -0.5\mathbf{R}_{12}''\frac{\partial\mathbf{R}_{22}''^{-1}}{\partial\theta}\mathbf{R}_{21}''\psi_1^2 \\ &\quad - \mathbf{R}_{23}'''\frac{\partial\mathbf{R}_{33}'''^{-1}}{\partial\theta}\big(\mathbf{R}_{31}'''\psi_1 + 0.5\mathbf{R}_{32}'''\psi_2\big)\psi_2 \end{aligned} \tag{77}$$

For a SRM operating with more than two phases conducting simultaneously, other integrals representing the stored energy or co-energy of the other excited phases are added to Eq. (74) and Eq. (72), respectively. Each extra integral maintains the current level of each phase whose corresponding stored energy or co-energy has been already considered by the last integrals, and builds up the current of the next phase.

8 Rotor skew

It has been shown that, using a set of 2-D FEM models corresponding to slices of a machine with skewed rotor poles, a good estimation of the machine characteristics can be obtained comparable with 3-D FEM results [12]. In this method, the slices have the same lengths as a fraction of the rotor length. Each characteristic of the machine is obtained from superposing the related results for the slices. So, using the new proposed model of a non-skewed machine, the results can be evaluated for the skewed machine by calculating a sum of the characteristics of the slices.

Table 1. Main parameters of the test SRM

Parameter description	Value
Stator outer diameter	215 (mm)
Stator yoke inner diameter	195 (mm)
Rotor diameter	146 (mm)
Rotor yoke outer diameter	94 (mm)
Shaft diameter	50 (mm)
Airgap length	0.3 (mm)
Stack length	200 (mm)
Number of rotor poles	8
Number of stator poles	12
Rotor pole arc	18 (deg)
Stator pole arc	13 (deg)
Number of winding turns	18 turns/pole
Number of pole per phase	4
Maximum current	400 (A)
DC supply voltage	220 (V)

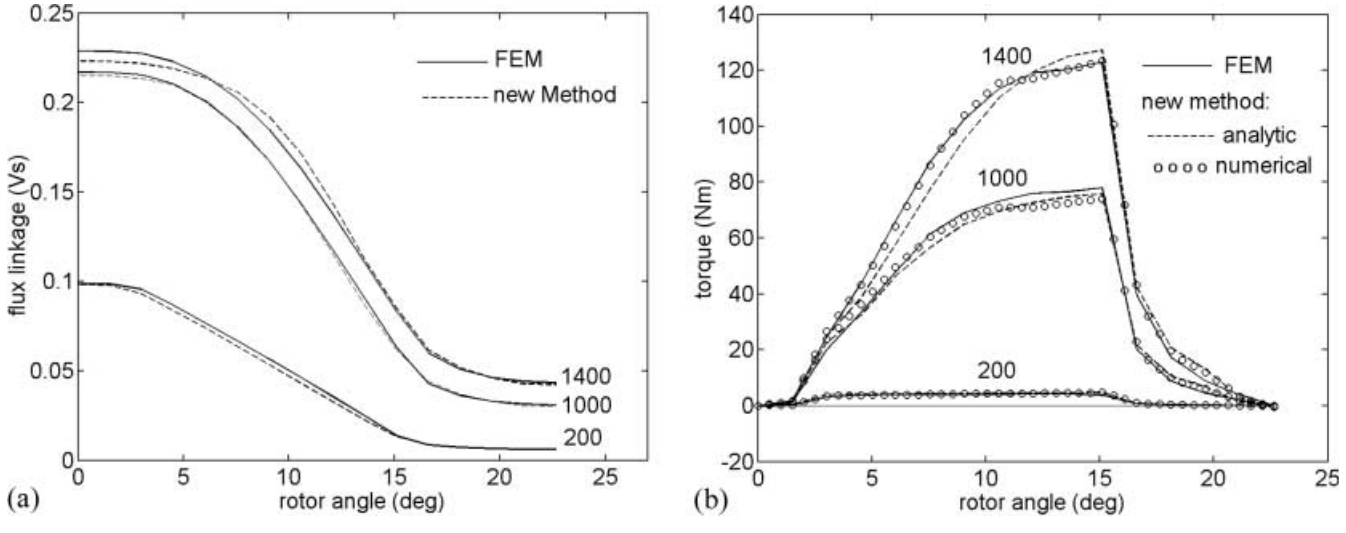

Fig. 15. Flux linkage (**a**) and static torque characteristics (**b**) for non-skewed machine

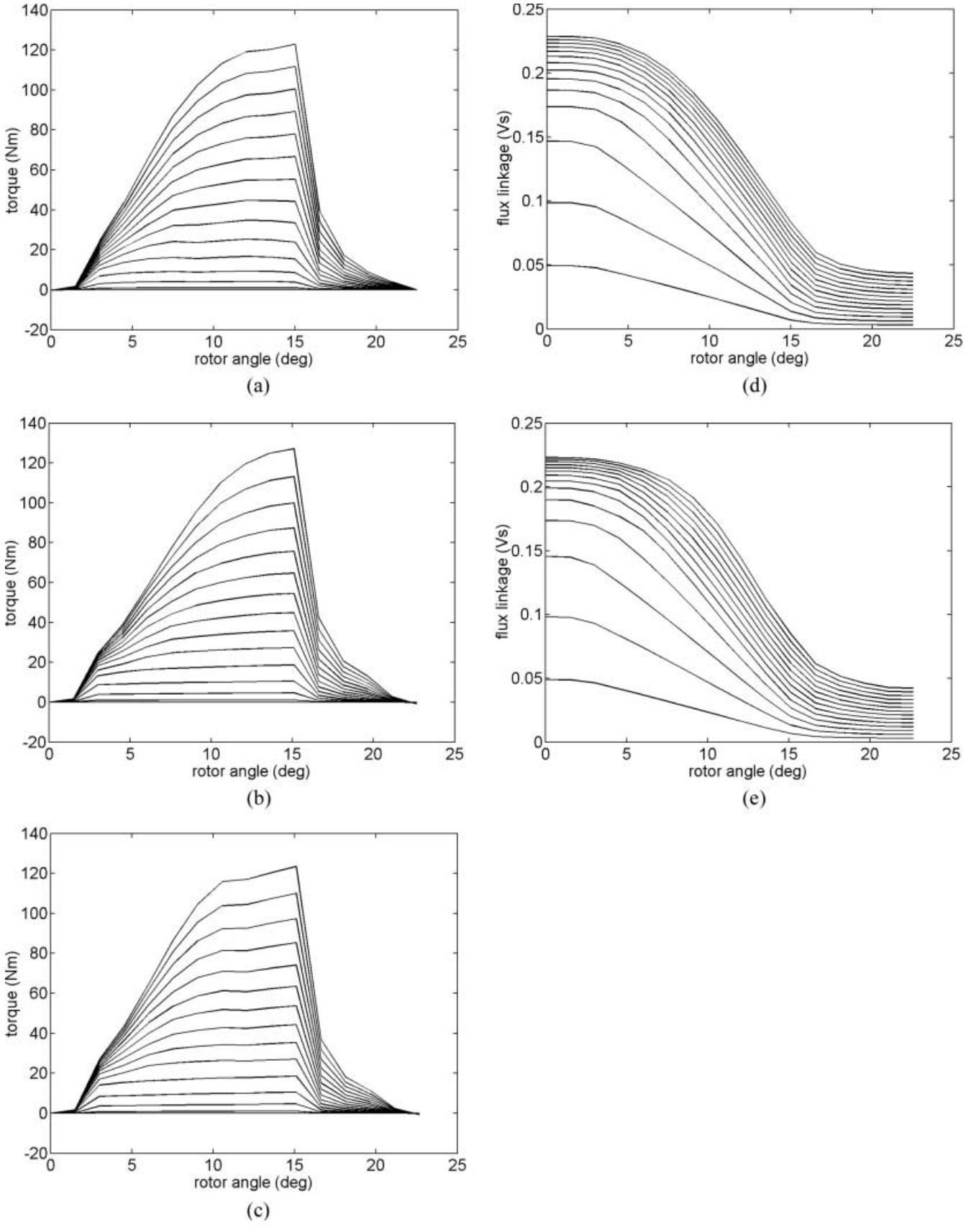

Fig. 16a–e. Flux linkage and static torque characteristics for non-skewed machine: **a** torque–FEM; **b** torque–new model analytic approach; **c** torque–new model numerical approach; **d** flux linkage–FEM; **e** flux linkage–new model

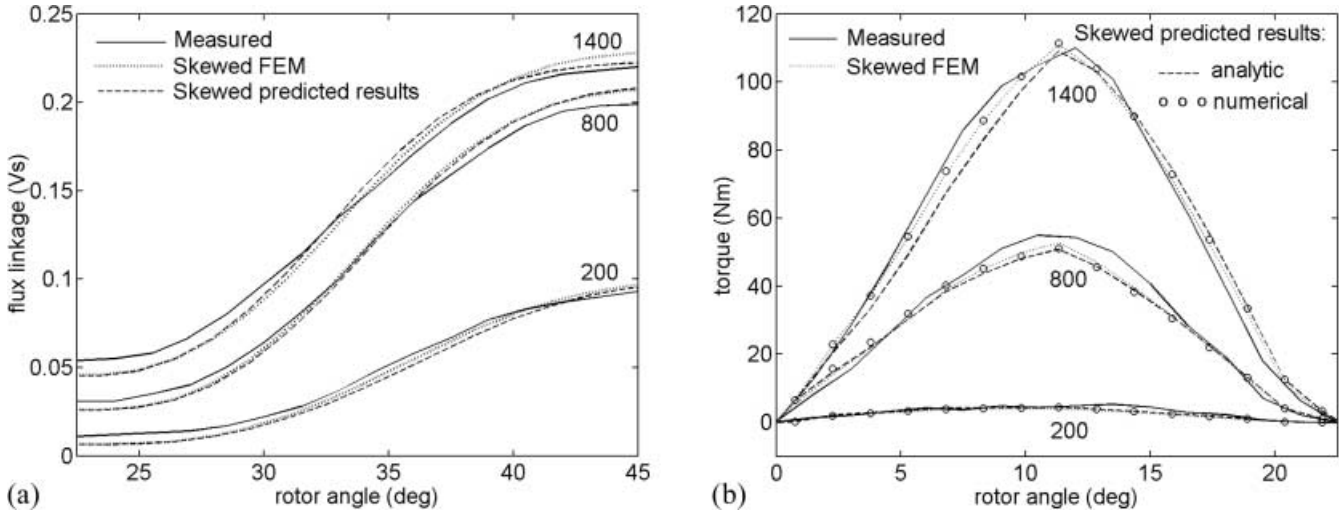

Fig. 17. Flux linkage (**a**) and static torque characteristics (**b**) for skewed machine

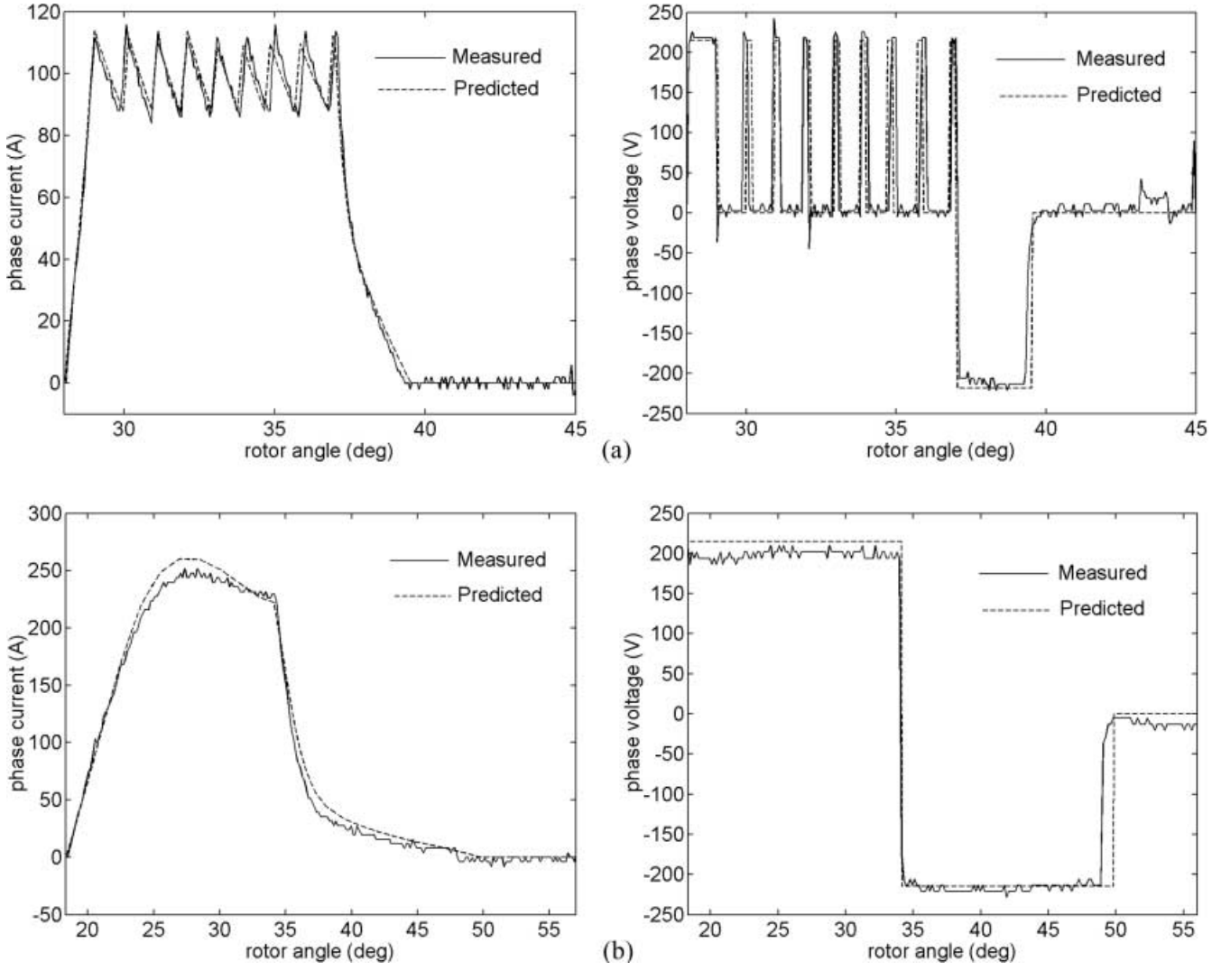

Fig. 18a, b. Phase current and voltage waveforms for working points of: **a** 500 rpm and 30 N m; **b** 3000 rpm and 100 N m

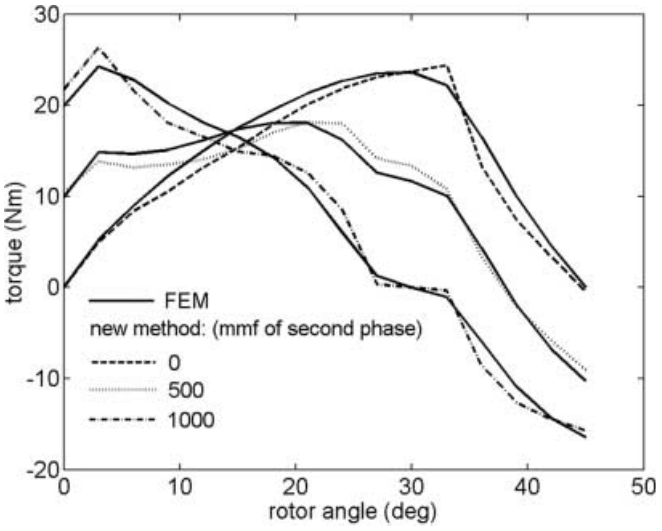

Fig. 19. Static torque characteristics of a 6/4 SRM for two phases conducted simultaneously

For dynamic analysis which has already been described, the circuit model is solved at each step of the rotation to determine the values of the mmf sources of the phases and, in turn, the values of the currents of the phases. So, the superposition of the results for the slices should be considered in the model equations for the dynamic analysis of a skewed machine.

In the case of one-phase excitation, Eq. (58) can be rewritten for the kth slice (k=1, ..., K) as follows:

$$\begin{bmatrix} {}^{k}\mathbf{R} \end{bmatrix} \begin{bmatrix} {}^{k}\psi_1 \\ {}^{k}\Phi' \end{bmatrix} = \begin{bmatrix} 1 \\ \mathbf{0} \end{bmatrix} Ni_1 \tag{78}$$

where:

$$\psi_1 = \sum_{k=1}^{K} {}^{k}\psi_1 \tag{79}$$

For all slices, the total set of equations can be accumulated into one matrix equation as in Eq. (80).

$$\begin{bmatrix} {}^{1}\mathbf{R} & & \\ & \ddots & \\ & & {}^{K}\mathbf{R} \end{bmatrix} \begin{bmatrix} {}^{1}\psi_1 \\ {}^{1}\Phi' \\ \vdots \\ {}^{K}\psi_1 \\ {}^{K}\Phi' \end{bmatrix} = \begin{bmatrix} 1 \\ 0 \\ \vdots \\ 1 \\ 0 \end{bmatrix} Ni_1 \tag{80}$$

By substitution of ${}^{1}\psi_1$ from Eq. (79) and some manipulations, Eq. (80) gives:

$$\begin{bmatrix} \mathbf{Z}_{11} & \mathbf{Z}_{12} \\ \mathbf{Z}_{21} & \mathbf{Z}_{22} \end{bmatrix} \begin{bmatrix} \psi_1 \\ \Phi'' \end{bmatrix} = \begin{bmatrix} 1 \\ \mathbf{0} \end{bmatrix} Ni_1 \tag{81}$$

This relation is perfectly similar to Eq. (58) and solved by the same method. So, the generalization of dynamic analysis for the skewed SRM with multiphase excitation is readily accomplished similarly to the case of the non-skewed machine.

9
Comparison of simulation and experimental results

The new model was applied to obtain the static characteristics of a 35-kW, three-phase, 12/8 SRM which was designed and constructed in the department of electrical machines of Aachen University [13]. The main parameters of the machine are given in Table 1. At first, the new model was compared with 2-D FE analysis for the non-skewed machine. The results for one phase excited by the constant mmf of 200, 1,000, and 1,400-A-turns are given in Fig. 15. Figure 15b includes the results for the static torque calculated using the analytic and numerical approaches of the new model. The numerical approach with $m = 8$ in Eq. (61) yields better results than the analytic approach, but it needs 16 times the solution of Eq. (52). More results are given in Fig. 16 for the constant mmf, increasing in 100-A-turn steps from 100 to 1,400-A turns. Close agreement between the results of FEM and the new model for the non-skewed machine is evident in all the cases. Figure 17 shows the comparative results of the static characteristics for the skewed machine. The measured values are compared with the skewed results obtained from 2-D FE analysis and the new model of the non-skewed machine. Because of the large length of the machine with respect to its external diameter, the end effects are negligible. Consequently, there is a close agreement between 3-D FEM results and the skewed results of 2-D FEM.

The results of dynamic simulation using the procedure described in Sect. 8 are shown in Fig. 18 for the new model against the measured results. The phase current and voltage waveforms are shown for two working points of 500 rpm, 30 N m and 3,000 rpm, 100 N m. The measured and predicted waveforms agree well. Finally, Fig. 19 shows the comparative results of the static torque characteristics of a 6/4 SRM for two phases conducting simultaneously. One phase is excited up to 1,000-A turns and another phase is excited up to 0, 500 and 1,000-A turns. The motivation to take this machine as an example is that the simultaneous excitation of two phases of this machine up to the same mmf value of 1,000-A turns causes saturation in the stator yoke of the machine. This is a direct result of the width of the stator yoke being smaller than half the stator pole width [11]. The modeling of the machine with the saturated stator yoke can best show the performance of the new model. As shown, the results for the new model and FE analysis are in good agreement.

Conclusion

A general nonlinear model of a SRM was introduced based on the concept of the magnetic equivalent circuit covering all possible flux paths in a 2-D view of the machine. The model includes the effects of mutual coupling between phases and multiphase excitation, representing an efficient analyzing tool for CAD and optimal design. New techniques were employed to model the stator and rotor poles and the rotor core. The analytic and numerical matrix procedures were addressed to calculate the machine torque. Dynamic simulation of the machine was formulated for machines with skewed and non-skewed rotor poles. Finally, the maturity of the model was verified by comparison of simulation with finite element analysis and measurements.

References

1. **Arumugam R** (1985) Magnetic field analysis of a switched reluctance motor using two dimension finite element model. IEEE Trans Magn 21:1883–1885
2. **Moallem M, Ong CM** (1991) Predicting the steady state performance of a switched reluctance motor. IEEE Trans Ind Appl 27:1087–1097
3. **Omekanda A, Broche C, Crappe M, Baland R** (1998) Prediction of the steady state performance of the switched reluctance motor using quadratic BIEM-FEM field solution in the linear model. ETEP Eur Trans Electr Power 8:5–10
4. **Mizia J, Adamiac K, Eastham AR, Dawson GE** (1988) Finite element force calculation: comparison of methods for electric machines. IEEE Trans Magn 24:447–450
5. **Miller TJE, McGilp M** (1990) Nonlinear theory of the switched reluctance motor for rapid computer-aided design. IEE Proc B 137:337–374
6. **Miller TJE, Glinka M, McGilp M, Cossar C, Gallegoes-Lopez G, Ionel D, Olaru M** (1998) Ultra-fast model of the switched reluctance motor. IEEE IAS Annual Meeting, St Louis
7. **Vujicic V, Vukosavic SN** (2000) A simple nonlinear model of the switched reluctance motor. IEEE Trans Energy Conv 15:395–400
8. **Moallem M, Dawson GE** (1998) An improved magnetic equivalent circuit method for predicting the characteristics of highly saturated electromagnetic devices. IEEE Trans Magn 34:3632–3635
9. **Preston MA, Lyons JP** (1991) A switched reluctance motor model with mutual coupling and multi-phase excitation. IEEE Trans Magn 27:5423–5425
10. **Kokernak JM, Torrey DA** (1997) Magnetic circuit model for the mutually coupled switched reluctance machine. IEEE IAS Annu Meet 1:302–309
11. **Michaelides AM, Pollock C** (1996) Modify and design of switched reluctance motors with two phases simultaneously excited. IEE Proc B 143:361–370
12. **Mueller MA** (1998) Switched reluctance machines with rotor skews. Proceedings of the International Conference on Electrical Machines, Espoo, Finland, 1680–1685
13. **Risse S, Henneberger G** (2000) Design and optimization of a switched reluctance motor for electric vehicle propulsion. Conference Proc ICEM:1526–1530